The SNR of time-of-flight positron emission tomography data for joint reconstruction of the activity and attenuation images

Johan Nuyts, Michel Defrise, Christian Morel, Paul Lecoq

October 2, 2023

Abstract

Objective. Measurement of the time-of-flight (TOF) difference of each coincident pair of photons increases the effective sensitivity of positron emission tomography (PET). Many authors have analyzed the benefit of TOF for quantification and hot spot detection in the reconstructed activity images. However, TOF not only improves the effective sensitivity, it also enables the joint reconstruction of the tracer concentration and attenuation images. This can be used to correct for errors in CT- or MR-derived attenuation maps, or to apply attenuation correction without the help of a second modality. This paper presents an analysis of the effect of TOF on the variance of the jointly reconstructed attenuation and (attenuation corrected) tracer concentration images. *Approach.* The analysis is performed for PET systems that have a distribution of possibly non-Gaussian TOF-kernels, and includes the conventional Gaussian TOF-kernel as a special case. Non-Gaussian TOF-kernels are often observed in novel detector designs, which make use of two (or more) different mechanisms to convert the incoming 511 keV photon to optical photons. The analytical result is validated with a simple 2D simulation. *Main results.* We show that if two different TOF-kernels are equivalent for image reconstruction with known attenuation, then they are also equivalent for joint reconstruction of the activity and the attenuation images. The variance increase in the activity, caused by also jointly reconstructing the attenuation image, vanishes when the TOF-resolution approaches perfection. *Significance.* These results are of interest for PET detector development and for the development of stand-alone PET systems.

1 Introduction

In the design of positron emission tomography (PET) systems, there is a clear tendency to a larger axial field of view and a better time-of-flight (TOF) resolution. Both of these increase the effective sensitivity of the system, enabling it to achieve a better compromise between dose reduction, scan time reduction and image quality improvement. In the last few years, the TOF-resolution of commercial time-of-flight systems has reduced from more than 500 ps to about 200 ps [1]. Recent papers on detector development promise further improvements

This work was supported in part by the Research Foundation - Flanders (FWO) under grant G062220N and by NIH/NIBIB grant P41EB017183, CAI^{2}R, New York University.

JN is with KU Leuven, University of Leuven, Department of Imaging and Pathology, Nuclear Medicine & Molecular imaging; Medical Imaging Research Center (MIRC), B-3000, Leuven, Belgium (e-mail: johan.nuyts@uzleuven.be). MD is with Department of Nuclear Medicine, Vrije Universiteit Brussel, B-1090, Brussels, Belgium (e-mail: michel.defrise@vub.be). CM is with Aix-Marseille Univ, CNRS/IN2P3, CPPM, Marseille, France, (e-mail: morel@cppm.in2p3.fr). PL is with Polytechnic University of Valencia, Spain (e-mail: paul.lecoq@metacrystal.ch).

and a very ambitious 10 ps TOF-resolution is believed to be achievable in principle [2]. However, pushing the TOF-resolution well below 100 ps will probably not be possible with conventional scintillation detection [3]. Two currently unconventional approaches are the use of Cherenkov photons in scintillation detectors [4–10] or non-scintillating detectors [11, 12], and metascintillators [13, 14]. PET systems with such detectors often have non-Gaussian TOF-kernels, and may even have a distribution of TOF-kernels, i.e. the TOF-resolution depends on the type of event [1].

For earlier and current commercial PET-systems, it is reasonable to assume that the TOF-kernel is Gaussian. In 1981, Tomitani [15] computed analytically how the variance in the reconstructed PET image depends on the width of a Gaussian TOF-kernel. He did the calculation for the center of a uniform cylinder, and for reconstruction with filtered backprojection. However, because of the circular symmetry, the results also apply to reconstruction with maximum-likelihood algorithms.

In [16], we have extended this analysis to PET systems that have a distribution of possibly non-Gaussian TOF-kernels, considering PET-systems that either can or cannot identify the TOF-kernel associated with each event. When applying this analysis to the special case of a conventional Gaussian TOF-kernel, it reproduces Tomitani's result. In addition, we found that up to a good approximation, the computed TOF-gain not only applies to the variance in the reconstructed image, but also to the detection performance for small hot spot detection in a signal-known-exactly background-known-exactly setup. This mathematical analysis was validated with simulation results.

In this paper, we propose a similar analysis, but now for the joint reconstruction of the tracer concentration (also called the activity) and the attenuation coefficients.

2 Methods

This section first briefly reviews the result obtained in [16], because the new analysis depends on it. Then, a detection experiment is proposed, designed (guided by intuition) to capture the essence of the joint estimation problem. This detection experiment produces an equation for the SNR of a Hotelling observer. In the third section, an analytical expression is derived to compute the variance in the center of the activity and attenuation images, for a TOF-PET scan of a uniform cylinder. For the activity image, the variance obtained by the latter analysis is inversely proportional to the squared SNR obtained from the detection experiment. The relation is slightly more complex for the variance on the reconstructed attenuation image.

In the analysis of [16], randoms and scatter were ignored, and the variance computations considered only 2D TOF-PET. The same is done is this paper. The inclusion of randoms and scatter is relatively straightforward, as is the extension to fully 3D PET with complete sampling over 4π. Extending the analysis for realistic 3D sampling patterns used in typical (almost) cylindrical PET systems will be more complicated.

2.1 Previous work for conventional reconstruction of the activity

The main result of [16] associates a signal-to-noise ratio (SNR) with a particular TOF-event type along a line-of-response (LOR). It is the SNR of the Hotelling observer, for detecting

[1] An event denotes the detection of a coincident photon pair. If the timing resolution with which a photon is detected can vary significantly from event to event, then the system has multiple TOF-kernels.

the presence or absence of a weak hot spot S at the center of the LOR. It can be written as

$$\mathrm{SNR}^2_{\lambda,\mathrm{TOF}} = e^{-\mu D}\, S^2 \int_{-\infty}^{\infty} \frac{k^2(x)}{(B \otimes k)(x)} dx \tag{1}$$

$$(B \otimes k)(x) = \int_{-\infty}^{\infty} B(\xi) k(x-\xi) d\xi \tag{2}$$

where $k(x)$ is the TOF-kernel, $B(x)$ is the background activity as a function of position x along the LOR, $\otimes$ denotes the convolution and S is the excess activity in the small hot spot, with $S \ll \int_{-\infty}^{\infty} B(x)dx$. The subscript λ denotes that this SNR is for reconstruction of the activity when the attenuation is known. The background activity $B(x)$ does not have to be uniform. In [16] the attenuation of the object was ignored. It was accounted for here, by multiplying the activities S and B with the attenuation $\exp(-\mu D)$, where D is the size of the object along the LOR and a uniform attenuation with the linear attenuation coefficient μ was assumed.

Note that the TOF-kernel $k(x)$ is a probability distribution; it gives the probability that the PET system will assign the event to position x along the LOR, given that the true location of the event is at center of the LOR ($x = 0$). This implies that $\int_{-\infty}^{\infty} k(x)dx = 1$.

If we introduce the additional assumptions that $B(x) = B$ is uniform in the object, and the object size D along the LOR is large compared to the width of the TOF kernel $k(x)$, then equation (1) simplifies to

$$\mathrm{SNR}^2_{\lambda,\mathrm{TOF}} = e^{-\mu D}\, \frac{S^2}{B} \int_{-\infty}^{\infty} k^2(x)dx. \tag{3}$$

On the other hand, if we assume instead that the TOF kernel is much larger than the object size D, i.e. we consider a non-TOF PET system, then equation (1) simplifies to

$$\mathrm{SNR}^2_{\lambda,\mathrm{nonTOF}} = e^{-\mu D}\, \frac{S^2}{BD}. \tag{4}$$

Consequently, for a uniform object, the SNR-gain obtained by going from TOF to non-TOF equals

$$\frac{\mathrm{SNR}^2_{\lambda,\mathrm{TOF}}}{\mathrm{SNR}^2_{\lambda,\mathrm{nonTOF}}} = D \int_{-\infty}^{\infty} k^2(x)dx. \tag{5}$$

Finally, we could show that with good approximation, equation (5) also holds for the variance-gain in the center of an image that was reconstructed from a noisy PET scan of a uniform cylinder [16]. In this case, it is essential that the TOF and non-TOF images are reconstructed with exactly the same spatial resolution (ensuring that they see the same signal on average, but with different variance). The computation is based on reconstruction with filtered backprojection, but because of the circular symmetry, it also holds for maximum-likelihood and (weighted) least squares reconstruction. Consequently, equation (5) is really a feature of the PET-data, independent of the reconstruction algorithm.

This result means that the integral of the squared TOF-kernel is a better metric for the value of a particular TOF-kernel than its standard deviation or full width at half maximum (FWHM). Comparing the FWHM of two TOF-kernels is only meaningful if these kernels have exactly the same shape.

As mentioned above, equation (5) reduces to Tomitani's variance gain [15] for a Gaussian TOF-kernel, given by

$$\frac{\mathrm{SNR}^2_{\lambda,\mathrm{TOFgauss}}}{\mathrm{SNR}^2_{\lambda,\mathrm{nonTOF}}} = \frac{\mathrm{VAR}_{\lambda,\mathrm{nonTOF}}}{\mathrm{VAR}_{\lambda,\mathrm{TOFgauss}}} = \sqrt{\frac{2\ln 2}{\pi}}\frac{D}{W} = 0.664\frac{D}{W} \tag{6}$$

where W is the FWHM of the Gaussian TOF-kernel (converted to unit of distance). This equation has been confirmed by simulations and phantom experiments [17–20]. In some other publications, the TOF-gain is said to equal D/W, but for good agreement with experiments, the non-negligible factor of 0.664 is essential.

2.2 A detection task for joint estimation

Joint estimation of the activity and attenuation from non-TOF-PET data is a highly ill-posed problem: the reconstructions often suffer from cross-talk [21, 22], which can only be suppressed with strong constraining [23]. Similar results were obtained for SPECT [21, 24, 25]. It is unclear to which extent this is due to non-uniqueness of the solution or to extremely slow convergence of the iterative algorithms for this problem. For objects with circularly symmetrical activity and attenuation, the problem has infinitely many solutions [26]. However, for irregular objects such as the human body, it is not clear if the solution is typically not unique. In 2D PET, non-uniqueness is the generic case for a smooth activity, but examples of non-smooth activity with a unique solution exist [27]. Some groups reported successful numerical inversion [28, 29], usually at the cost of a high number of iterations, indicating that at least for some images, the solution is (almost) unique, although potentially unstable for noisy data .

On the other hand, TOF-PET data with sufficiently high TOF resolution enable stable joint estimation [30–33], and the stability improves with improving TOF resolution. The cross-talk in reconstruction from non-TOF-PET data indicates that the same change in the data can be explained by changing either the activity or the attenuation. Here, a detection experiment that focuses on this cross-talk problem is proposed.

Consider an LOR going through the center of a uniform cylinder. The cylinder has an activity of B per unit distance along the LOR, a linear attenuation coefficient μ and diameter D. In the center, we may add a small amount of activity S, in combination with a small increase ϕ of the attenuation along the LOR. This change to the attenuation can be written as $\phi = e^{-S_\mu}$, where S_μ represents the integral of the change to the linear attenuation coefficients along the LOR. At this point, it does not matter where the attenuation was changed along the LOR. We assume that S and S_μ are small, such that $|S| \ll BD$, $|S_\mu| \ll \mu D$ and $\phi \simeq 1 - S_\mu$.

In the following we compute the performance of the Hotelling observer for detecting if that change to activity and attenuation was present or not, for a non-TOF and TOF PET system. We assume the observer knows the expectation of the measurements under both hypotheses, the only things unknown are the noise and the presence or absence of the change (S, S_μ). Consequently, this is a signal known exactly / background known exactly (SKE/BKE) experiment [34].

2.2.1 non-TOF-PET

For the non-TOF PET case, the expectation of the measured count y equals

$$\begin{aligned} E(y|H_0) &= BDe^{-\mu D} \\ E(y|H_1) &\simeq (BD + S)e^{-\mu D}(1 - S_\mu) \end{aligned} \tag{7}$$

where H_0 and H_1 denote the (S, S_μ) absent and present conditions, respectively. The variance on the measurement equals $e^{-\mu D}BD$, because y is subject to Poisson noise and S and S_μ are

very small. The squared SNR for the detection task equals

$$\begin{aligned}\mathrm{SNR}^2_{\mathrm{joint,nonTOF}} &= \frac{(E(y|H_1) - E(y|H_0))^2}{e^{-\mu D}BD} \\ &\simeq e^{-\mu D}\left(BDS_\mu^2 + \frac{S^2}{BD} - 2SS_\mu\right)\end{aligned} \tag{8}$$

where we ignored higher orders of S and S_μ. This SNR becomes zero when

$$S_\mu = \frac{S}{BD} \tag{9}$$

because with this choice, the slight increase of the activity with S is perfectly compensated by the slight increase of the attenuation with S_μ, as revealed by inserting (9) in (8).

2.2.2 TOF-PET

TOF-PET produces a measured count profile y, obtained in a number of bins along the LOR. For the measurement with the unchanged phantom, this profile equals the true profile convolved with the TOF-kernel $k(x)$. Using the continuous model this can be written as:

$$E(y(x)|H_0) = e^{-\mu D}\int_{-\infty}^{\infty} B(\xi)k(x-\xi)d\xi = e^{-\mu D}(B \otimes k)(x). \tag{10}$$

For the phantom changed with (S, S_μ) one finds

$$\begin{aligned}E(y(x)|H_1) &= e^{-\mu D}((B \otimes k)(x) + Sk(x))\ (1 - S_\mu) \\ &\simeq e^{-\mu D}((B \otimes k)(x) + Sk(x) - S_\mu(B \otimes k)(x))\end{aligned} \tag{11}$$

where we ignored the second order term in SS_μ.

One can show that for this SKE/BKE experiment, the squared SNR of the Hotelling observer is given by [34]

$$\mathrm{SNR}^2 = \bar{s}^T V^{-1}\bar{s} \tag{12}$$

$$\bar{s} = E(y|H_1) - E(y|H_0) \tag{13}$$

$$V = \mathrm{diag}(\bar{y}) \simeq \mathrm{diag}(E(y|H_0)) \tag{14}$$

where $\bar{s}$ is the expectation of the induced change to the measurement y. Because the Poisson noise on y is uncorrelated, the covariance V is diagonal. And because S and S_μ are very small, the variance on y is the same under both hypotheses. Inserting (10) and (11), we obtain

$$\begin{aligned}\mathrm{SNR}^2_{\mathrm{joint}} &= \int_{-\infty}^{\infty}\frac{\bar{s}^2(x)}{V(x)}dx \\ &\simeq e^{-\mu D}\int_{-\infty}^{\infty}\left(S^2\frac{k^2(x)}{(B \otimes k)(x)} - 2SS_\mu k(x) + S_\mu^2(B \otimes k)(x)\right)dx \\ &= e^{-\mu D}\left(S^2\int_{-\infty}^{\infty}\frac{k^2(x)}{(B \otimes k)(x)}dx - 2SS_\mu + S_\mu^2 BD\right)\end{aligned} \tag{15}$$

where we used $\int_{-\infty}^{\infty} k(x)dx = 1$ and $\int_{-\infty}^{\infty}(B \otimes k)(x)dx = BD$. As in the non-TOF case (9), the minimum is obtained for $S_\mu = S/(BD)$, producing:

$$\mathrm{SNR}^2_{\mathrm{joint}} \simeq e^{-\mu D}S^2\int_{-\infty}^{\infty}\frac{k^2(x)}{(B \otimes k)(x)}dx - e^{-\mu D}\frac{S^2}{BD} \tag{16}$$

Using equations (1) and (4) and accounting for the attenuation $\exp(-\mu D)$ by the uniform object, equation (16) can be rewritten as

$$\mathrm{SNR}^2_{\mathrm{joint}} = \mathrm{SNR}^2_{\lambda,\mathrm{TOF}} - \mathrm{SNR}^2_{\lambda,\mathrm{nonTOF}} \tag{17}$$

Note that in this equation, $\mathrm{SNR}_{\mathrm{joint}}$ is the SNR for the new detection experiment that aims to model the cross-talk problem in joint estimation, whereas $\mathrm{SNR}_{\lambda,\mathrm{TOF}}$ and $\mathrm{SNR}_{\lambda,\mathrm{nonTOF}}$ are for detection of an activity hot spot when the attenuation is known.

2.3 The variance in joint reconstruction of activity and attenuation

To obtain an estimate of the variance in the reconstructed images, we will assume that image reconstruction computes the (post-smoothed) minimum-norm weighted least-squares reconstruction. With this approximation, the covariance matrix can be computed as the (pseudo-) inverse of the Fisher information matrix. From the covariance matrix, the variance on the reconstructed pixel values is computed. Following [15, 16], the derivation is done for 2D TOF-PET.

2.3.1 The Fisher information matrix for joint reconstruction

The PET model considered here can be written as

$$a_i = e^{-\sum_j l_{ij}\mu_j} \tag{18}$$

$$\bar{y}_i = a_i \sum_j c_{ij}\lambda_j \tag{19}$$

$$\bar{y}_{it} = a_i \sum_j c_{ijt}\lambda_j \tag{20}$$

$$L_{\mathrm{nonTOF}} = \sum_i y_i \ln \bar{y}_i - \bar{y}_i \tag{21}$$

$$L_{\mathrm{TOF}} = \sum_{it} y_{it} \ln \bar{y}_{it} - \bar{y}_{it} \tag{22}$$

where λ is is the activity image and μ the attenuation image, both represented as column matrices. The expectations of the TOF and non-TOF PET measurements are $\bar{y}_{it}$ and $\bar{y}_i = \sum_t \bar{y}_{it}$; c_{ijt} and $c_{ij} = \sum_t c_{ijt}$ are the TOF and non-TOF projection matrix elements for the activity, and l_{ij} are the projection matrix elements for the attenuation. The LOR-index is i, j is the voxel-index in the image and t the TOF-index along the LOR. The attenuation along LOR i is a_i. L_{nonTOF} and L_{TOF} are the non-TOF and TOF log-likelihood functions.

The joint Fisher information matrix for estimating $\psi^T = [\lambda^T, \mu^T]^T$ can be written as a block matrix:

$$F = \begin{bmatrix} F_{\lambda\lambda} & F_{\lambda\mu} \\ F_{\lambda\mu} & F_{\mu\mu} \end{bmatrix} = \begin{bmatrix} -E\left(\frac{\partial^2 L}{\partial\lambda\partial\lambda}\right) & -E\left(\frac{\partial^2 L}{\partial\lambda\partial\mu}\right) \\ -E\left(\frac{\partial^2 L}{\partial\lambda\partial\mu}\right) & -E\left(\frac{\partial^2 L}{\partial\mu\partial\mu}\right) \end{bmatrix} \tag{23}$$

where $E(x)$ is the expectation of x. $F_{\lambda\lambda}$ is the Fisher information matrix for estimating the activity λ from the data y, given the attenuation a. The Fisher information matrix (FIM) elements for TOF-PET are

$$E\left(\frac{\partial^2 L_{\mathrm{TOF}}}{\partial\lambda_j\partial\lambda_k}\right) = -\sum_{it} c_{ijt}c_{ikt}\frac{a_i^2}{\bar{y}_{it}} \tag{24}$$

The corresponding FIM elements for non-TOF-PET are

$$E\left(\frac{\partial^2 L_{\text{nonTOF}}}{\partial\lambda_j\partial\lambda_k}\right) = -\sum_i c_{ij}c_{ik}\frac{a_i^2}{\bar{y}_i} \tag{25}$$

The other two matrix blocks of the joint FIM are

$$E\left(\frac{\partial^2 L_{\text{TOF}}}{\partial\lambda_j\partial\mu_k}\right) = \sum_i c_{ij}l_{ik}a_i \tag{26}$$

$$E\left(\frac{\partial^2 L_{\text{TOF}}}{\partial\mu_j\partial\mu_k}\right) = -\sum_i l_{ij}l_{ik}\bar{y}_i \tag{27}$$

For TOF-PET, only $F_{\lambda\lambda}$ involves TOF projection and backprojection, the other three blocks of the FIM use only non-TOF system matrix elements.

2.3.2 The pseudo-inverse of the Fisher information matrix

In the following, several approximations are introduced, in the same spirit as was done for the extension of Tomitani's method in [16]. We consider a PET scan of a uniform cylinder with diameter D, which is large compared to the TOF resolution. We focus on the center of the cylinder, such that the problem becomes circularly symmetrical. The cylinder has activity B per unit length along central LORs. In addition, we assume that near the center, everything can be approximated as locally shift invariant.

We assume that the system matrix elements for the activity and attenuation projection are identical: $c_{ij} = l_{ij}$. Because of circular symmetry and the focus on the center, the factors a_i and $1/\bar{y}_i$ can be treated as independent of i. As a result, we can rewrite the FIM blocks as a function of the TOF or non-TOF FIMs for estimating the activity:

$$a_i = a \quad = e^{-\mu D} \tag{28}$$

$$\bar{y}_i = aBD \tag{29}$$

$$\beta = \frac{\bar{y}_i}{a_i} \quad = BD \tag{30}$$

$$T = F_{\lambda\lambda}^{\text{TOF}} \tag{31}$$

$$N = F_{\lambda\lambda}^{\text{nonTOF}} \tag{32}$$

$$F_{\lambda\mu} = -\beta N \tag{33}$$

$$F_{\mu\mu} = \beta^2 N \tag{34}$$

$$F = \begin{bmatrix} F_{\lambda\lambda} & F_{\lambda\mu} \\ F_{\lambda\mu} & F_{\mu\mu} \end{bmatrix} = \begin{bmatrix} T & -\beta N \\ -\beta N & \beta^2 N \end{bmatrix} \tag{35}$$

It is reasonable to assume that T and N are invertible for PET systems with complete sampling; in practice the reconstructions will be post-smoothed to suppress the noise, which stabilizes this (approximate) inversion. Assuming first that $T - N$ is also invertible, the covariance matrix for the joint estimation can be computed (with Gaussian elimination):

$$\begin{aligned} \text{Covar} = F^{-1} &= \begin{bmatrix} T & -\beta N \\ -\beta N & \beta^2 N \end{bmatrix}^{-1} \\ &= \begin{bmatrix} (T-N)^{-1} & \frac{1}{\beta}(T-N)^{-1} \\ \frac{1}{\beta}(T-N)^{-1} & \frac{1}{\beta^2}((T-N)^{-1} + N^{-1}) \end{bmatrix} \end{aligned} \tag{36}$$

Unfortunately, it can be shown that the matrix $T - N$ is always singular. To prove this, it is sufficient to find a vector u such that $(T - N)u = 0$ with $||u|| > 0$. Such a vector is obtained by taking $u_k = \eta\lambda_k$, with $\eta > 0$. Using equations (31), (32), (24) and (25) one obtains

$$(Tu)_j = \sum_k T_{jk}u_k = -\sum_k \sum_{it} c_{ijt}c_{ikt}\frac{a_i^2}{\bar{y}_{it}}\eta\lambda_k = -\eta\sum_{it} c_{ijt}\frac{a_i^2}{\bar{y}_{it}}\frac{\bar{y}_{it}}{a_i} = -\eta\sum_i c_{ij}a_i \tag{37}$$

$$(Nu)_j = \sum_k N_{jk}u_k = -\sum_k \sum_i c_{ij}c_{ik}\frac{a_i^2}{\bar{y}_i}\eta\lambda_k = -\eta\sum_i c_{ij}\frac{a_i^2}{\bar{y}_i}\frac{\bar{y}_i}{a_i} = -\eta\sum_i c_{ij}a_i \tag{38}$$

and therefore $(T - N)u = 0$. This result is not surprising, because the time-of-flight only determines the attenuation up to a constant [31]. The fact that this allows for infinitely many solutions implies that the Fisher information matrix is not invertible.

Assuming that the reconstruction will select the minimum-norm solution, we proceed by using the pseudo-inverse $F^\dagger$ instead of the inverse. One way to obtain it, is to replace $(T - N)^{-1}$ with $(T - N)^\dagger$ and verify if the result satisfies the pseudo-inverse properties $FF^\dagger F = F$ and $F^\dagger FF^\dagger = F^\dagger$. This verification is required because this approach does not produce a valid pseudoinverse in general, but it happened to do so in this case. Consequently, we have

$$\text{Covar} = F^\dagger = \begin{bmatrix} (T-N)^\dagger & \frac{1}{\beta}(T-N)^\dagger \\ \frac{1}{\beta}(T-N)^\dagger & \frac{1}{\beta^2}((T-N)^\dagger + N^{-1}) \end{bmatrix} \tag{39}$$

The top-left covariance sub-matrix in (39), $(T-N)^\dagger$, is the covariance between the pixel values in the activity image (at least near the center of the image). Similarly, the bottom-right sub-matrix $\frac{1}{\beta^2}(T - N)^\dagger + N^{-1}$ is the covariance between the pixel values in the reconstructed attenuation pixel values.

2.3.3 The variance in the post-smoothed reconstructed images

In the following, an extended version of Tomitani's analytical approach [15] is applied to compute the variance in the center of the activity and attenuation images, reconstructed from the TOF-PET sinogram of a uniform phantom. The reconstruction is done with a finite resolution to ensure a finite variance: a Gaussian point spread function with a predefined FWHM is imposed [15, 16].

Because all parameters $\{\lambda, \mu\}$ are estimated from the same noisy TOF-PET sinogram, their values are not statistically independent. The FIM element $F_{i,j}$ gives the amount of information that the estimated parameter j carries about parameter i. The elements $F_{i,j}$ on row i correspond to an image that represents the distribution of the information about pixel i. The Fisher information matrix is obviously very large, and all its rows are different, because each pixel is affected by different amounts of activity, attenuation, detector sensitivity etc. Inverting such a matrix is not feasible. As discussed in [35–38], $F_{i,j}$ decreases with increasing distance between the pixels i and j, and although all rows are different, the changes from one row to the next are typically small. In other words, the FIM row i represents a blob centered at i, and the corresponding blobs of pixels close to i are very similar. Consequently, when focusing on pixel i, it is acceptable to assume that all these blobs are identical. This shift-invariance assumption makes the FIM circulant, and circulant matrices can be inverted using the Fourier transform [38].

Following Tomitani, the calculations are done using a continuous model. It treats T and N as operators which map one image to another image, which is obtained with forward projection, division and backprojection. Because of the shift-invariance assumption, these

operators become convolutions. Discrete versions of the (convolution) operators T and N are given by equations (24) and (25). Since we will need the inverse, it is convenient to compute the operators in the Fourier domain. Using continuous expressions, the TOF operator can be written as

$$\hat{T}(R) = \frac{a^2}{aB}\mathcal{R}[K^*K](R) \tag{40}$$

where K is the Fourier transform of the TOF-kernel k, R is the radial coordinate (distance to the origin) in the 2D Fourier domain, $a = e^{-\mu D}$ is the attenuation and B is the activity per unit length along the LOR [15, 16]. Treating the data variance as a constant equal to aB is only valid if we can assume that the diameter of the cylinder D is large compared to the width of TOF kernel k. Finally, $\mathcal{R}$ is the 2D rotational mean operator [15]; for a 2D function $\varphi(x, y) = \varphi(y)$ that changes in one direction only, it can be defined as

$$\mathcal{R}[\varphi](R) = \frac{1}{\pi}\int_{-\pi/2}^{\pi/2} \varphi(R\sin\theta)d\theta \tag{41}$$

In (40) K and a implement TOF-blurring and attenuation along the LOR during projection, K^* the (adjoint) blurring during backprojection, aB corresponds to the data variance (i.e. $\bar{y}_{it}$ in (24)) and $\mathcal{R}$ computes the backprojection (assuming circular symmetry). Inserting (41) in (40) produces

$$\begin{aligned}
\hat{T}(R) &= \frac{a}{\pi B}\int_{-\pi/2}^{\pi/2}[K^*K](R\sin\theta)d\theta \\
&\simeq \frac{a}{\pi B}\int_{-\infty}^{\infty}[K^*K](R\theta)d\theta \\
&= \frac{a}{\pi B\,R}\int_{-\infty}^{\infty}[K^*K](\theta)d\theta \\
&= \frac{a}{\pi B\,R}\int_{-\infty}^{\infty}k^2(x)dx.
\end{aligned} \tag{42}$$

The second expression is obtained by approximating $\sin\theta$ with its linear approximation around $\theta = 0$. This is justified because K^*K has the shape of a low pass filter, such that the integral is dominated by the contribution from small values of the argument $R\sin\theta$. This approximation is discussed in more detail in [16]. For the same reason, the integration interval can be extended to infinity. The last equation follows from Parseval's identity.

For the non-TOF operator, the same computation is done, replacing K^*K with Dirac's δ, and using aBD as the data variance:

$$\begin{aligned}
\hat{N}(R) &= \frac{a}{BD}\mathcal{R}[\delta](R) \\
&= \frac{a}{\pi BD}\int_{-\pi/2}^{\pi/2}\delta(R\sin\theta)d\theta \\
&= \frac{a}{\pi BD}\int_{-\pi/2}^{\pi/2}\frac{\delta(\theta)}{|R\cos 0|}d\theta \\
&= \frac{a}{\pi BDR}
\end{aligned} \tag{43}$$

where we used $\delta f(x) = \delta(x - x_0)/|f'(x_0)|$ for a function f with $f(x_0) = 0$ and with first derivative f'.

The Fourier transform of the covariance is obtained by inverting $[\hat{T} - \hat{N}](R)$ and multiplying with the squared 2D Fourier transform of the Gaussian post-smoothing P. This post-smoothing is required, because unless a finite spatial resolution is imposed, the variance will become infinite [15]. In this covariance computation, the smoothing operation appears squared in the Fourier transform (see eq (9) in [15]).

The variance V_λ is obtained as the integral of that result:

$$\begin{aligned} V_\lambda &= 2\pi \int_0^\infty \frac{P^2(R)}{\hat{T}(R) - \hat{N}(R)} R\, dR \\ &= \frac{2\pi^2 B}{a \int_{-\infty}^{\infty} k^2(x)dx - \frac{a}{D}} \int_0^\infty e^{-4\pi^2\sigma_p^2 R^2} R^2\, dR \\ &= \frac{B}{a \int_{-\infty}^{\infty} k^2(x)dx - \frac{a}{D}} \frac{1}{16\sqrt{\pi}\sigma_p^3} \end{aligned} \tag{44}$$

For the last equality, we used $\int_0^\infty e^{-u}\sqrt{u}\, du = \sqrt{\pi}/2$.

Note that earlier, the inverse did not exist and had to be replaced by the pseudo-inverse, whereas here a meaningful result is obtained by using the inverse. The reason must be that by assuming shift invariance, the singularity has been eliminated.

A similar calculation is done for the variance in the center of the reconstructed attenuation image, again using the inverse instead of the pseudo-inverse. It is easy to verify that $(T - N)^{-1} + N^{-1} = (N - NT^{-1}N)^{-1}$. Proceeding as above one obtains

$$\begin{aligned} V_\mu &= \frac{2\pi}{\beta^2} \int_0^\infty \frac{P^2(R)}{\hat{N}(R) - \frac{\hat{N}^2(R)}{\hat{T}(R)}} R\, dR \\ &= \frac{2\pi}{a\beta^2} \int_0^\infty \frac{P^2(R)}{\frac{1}{\pi BD} - \frac{1}{\pi BD^2 \int_{-\infty}^{\infty} k^2(x)dx}} R^2\, dR \\ &= \frac{2\pi^2}{a\beta^2} \frac{1}{\frac{1}{BD}\left(1 - \frac{1}{D\int_{-\infty}^{\infty} k^2(x)dx}\right)} \int_0^\infty P^2(R) R^2\, dR \\ &= \frac{1}{\beta^2 \frac{a}{BD}\left(1 - \frac{1/D}{\int_{-\infty}^{\infty} k^2(x)dx}\right)} \frac{1}{16\sqrt{\pi}\sigma_p^3} \end{aligned} \tag{45}$$

To facilitate the comparison of the two variances, the relative variances $\tilde{V}_\lambda$ and $\tilde{V}_\mu$ are defined as

$$\tilde{V}_\lambda = \frac{V_\lambda}{B^2} \tag{46}$$

$$\tilde{V}_\mu = V_\mu D^2, \tag{47}$$

Their ratio equals

$$\frac{\tilde{V}_\lambda}{\tilde{V}_\mu} = \frac{1}{D\int_{-\infty}^{\infty} k^2(x)dx} \tag{48}$$

2.3.4 Connection between the SNR of the detection task and the image variances

The variances in the center of the reconstructed activity and attenuation images can be rewritten as a function of the SNR for the detection task. Using (3), (4) and (17), the

variance in the activity image (44) can be rewritten as

$$V_\lambda = \frac{B}{a\int_{-\infty}^{\infty} k^2(x)dx - \frac{a}{D}} \frac{1}{16\sqrt{\pi}\sigma_p^3} = \frac{S^2}{\mathrm{SNR}^2_{\mathrm{joint}}} \frac{1}{16\sqrt{\pi}\sigma_p^3} \tag{49}$$

The use of (3) and (17) implies (again) that this result only holds if the TOF-kernel is small compared to the diameter of the cylinder. The variance in the center of the attenuation image can be rewritten as

$$V_\mu = \frac{1}{\beta^2 \frac{a}{BD}\left(1 - \frac{1/D}{\int_{-\infty}^{\infty} k^2(x)dx}\right)} \frac{1}{16\sqrt{\pi}\sigma_p^3} = \frac{S_\mu^2}{\mathrm{SNR}^2_{\mathrm{joint},\mu}} \frac{1}{16\sqrt{\pi}\sigma_p^3} \tag{50}$$

where we used $S_\mu = S/(BD) = S/\beta$ as in (9), and defined $\mathrm{SNR}^2_{\mathrm{joint},\mu}$ as

$$\begin{aligned}\mathrm{SNR}^2_{\mathrm{joint},\mu} &= \mathrm{SNR}^2_{\lambda,\mathrm{nonTOF}}\left(1 - \frac{\mathrm{SNR}^2_{\lambda,\mathrm{nonTOF}}}{\mathrm{SNR}^2_{\lambda,\mathrm{TOF}}}\right) \\ &= \frac{\mathrm{SNR}^2_{\lambda,\mathrm{nonTOF}}}{\mathrm{SNR}^2_{\lambda,\mathrm{TOF}}} \mathrm{SNR}^2_{\mathrm{joint}}.\end{aligned} \tag{51}$$

For the ratio of the variances one finds

$$\frac{\tilde{V}_\lambda}{\tilde{V}_\mu} = \frac{V_\lambda}{S^2}\frac{S_\mu^2}{V_\mu} = \frac{\mathrm{SNR}^2_{\mathrm{joint},\mu}}{\mathrm{SNR}^2_{\mathrm{joint}}} = \frac{\mathrm{SNR}^2_{\lambda,\mathrm{nonTOF}}}{\mathrm{SNR}^2_{\lambda,\mathrm{TOF}}} \tag{52}$$

The relative variance in the activity image is inversely proportional to $\mathrm{SNR}^2_{\mathrm{joint}}$. The relative variance in the attenuation image is always higher, because $\mathrm{SNR}^2_{\lambda,\mathrm{TOF}} \geq \mathrm{SNR}^2_{\lambda,\mathrm{nonTOF}}$. While a TOF measurement along a single LOR already provides information about the activity at the location of interest, it only provides information about the total attenuation along that LOR. Consequently, to obtain the attenuation at the location of interest, it must be reconstructed from measurements along all LORs. This is essentially a non-TOF reconstruction. Thus, the variance on the reconstructed attenuation is affected by the variance on the estimated activity, and by the variance from the non-TOF reconstruction of the attenuation, based on that activity estimate. This interpretation corresponds to the relation

$$\frac{1}{\mathrm{SNR}^2_{\mathrm{joint},\mu}} = \frac{1}{\mathrm{SNR}^2_{\mathrm{joint}}} + \frac{1}{\mathrm{SNR}^2_{\lambda,\mathrm{nonTOF}}} \tag{53}$$

where $\mathrm{SNR}_{\lambda,\mathrm{nonTOF}}$ not only gives the SNR for the non-TOF detection of S when the attenuation is known exactly, it also equals the SNR for the non-TOF detection of S_μ when the activity is known exactly. Equation (53) clearly reflects the fourth block of the inverse of the FIM, equation (36).

2.3.5 Application to a distribution of possibly non-Gaussian TOF-kernels

Equations (44) and (45) hold for a PET system with TOF-kernel $k(x)$ of any shape. However, PET systems may detect photon pairs with an event-dependent TOF-kernel. In that situation, the SNR provided by the TOF-kernels depends on whether the system can assign the correct TOF-kernel to each event or not.

If the acquisition system is unable to identify the TOF-kernel associated to each event, then one can only account for the average TOF-kernel. This kernel is computed as the

probability-weighted average of all possible TOF-kernels [16]. This will typically produce a non-Gaussian TOF-kernel $k(x)$, and the corresponding SNR^2 or image variances can be computed directly with (44) and (45).

On the other hand, if the TOF-kernel associated with each event can be identified, then the appropriate kernel can be used for each event during image reconstruction. This additional information increases the SNR of the TOF-PET system. Assume that there are two different TOF-kernels $k_a(x)$ and $k_b(x)$, which have probabilities p_a and p_b, with $p_a + p_b = 1$. The TOF image is now reconstructed from two data sets, one with TOF-kernel $k_a(x)$ and one with TOF-kernel $k_b(x)$. Accordingly, the system matrix used during reconstruction will include both TOF-kernels. This implies that the TOF operator $\hat{T}(R)$ in (40) can be rewritten as a sum of two operators, one for each TOF-kernel:

$$\hat{T}(R) = p_a \hat{T}_a(R) + p_b \hat{T}_b(R). \tag{54}$$

Propagating this through the computation of V_λ, one finds that the denominator in (44) changes as follows:

$$\int_{-\infty}^{\infty} k^2(x)dx - \frac{1}{D} \quad \rightarrow \quad p_a \left(\int_{-\infty}^{\infty} k_a^2(x)dx - \frac{1}{D} \right) + p_b \left(\int_{-\infty}^{\infty} k_b^2(x)dx - \frac{1}{D} \right) \tag{55}$$

and therefore the joint SNR becomes:

$$\mathrm{SNR}^2_{\mathrm{joint}}(p_a, k_a, p_b, k_b) \;=\; p_a \, \mathrm{SNR}^2_{\mathrm{joint}}(k_a) + p_b \, \mathrm{SNR}^2_{\mathrm{joint}}(k_b). \tag{56}$$

This means that the SNR^2 of a PET system with different and identified TOF-kernels simply equals the weighted arithmetic mean of the SNR^2 associated with each event. And consequently, the variance is obtained as the (weighted) harmonic mean of the variances for each kernel. The same feature was obtained for the SNR^2 and variances for conventional reconstruction with known attenuation [16]. There it was also shown that for the same distribution of events, the SNR is always higher if the TOF-kernel can be identified for each event.

However, simply averaging squared SNRs does not work for the attenuation image, because $\mathrm{SNR}^2_{\mathrm{joint},\mu}$ is not a linear function of $\int_{-\infty}^{\infty} k^2(x)dx$. Consequently, to compute the SNR and variance for the attenuation image, one must first compute $\mathrm{SNR}^2_{\mathrm{joint}}(p_a, k_a, p_b, k_b)$ using the weighted mean as explained above, and then use (51) and (45) to compute the corresponding SNR and variance for the attenuation image.

3 Experiments

A 2D simulation experiment was done to verify the results obtained above, using multiple noise realizations to estimate the variance in the reconstructed images. The observed variances in the activity and attenuation images are compared to their predictions by (44), (45) and (48), for different TOF resolutions. The reconstruction is done with MLAA, the maximum-likelihood algorithm for activity and attenuation [32]. This algorithm alternates between updating the activity image with MLEM and the attenuation image with MLTR, a maximum likelihood algorithm for transmission tomography. Because the convergence of the activity image is accelerated by TOF, whereas the update of the attenuation image is not, we typically apply multiple MLTR updates for a single MLEM update. MLAA was initialized with uniform images. To deal with the unknown constant [31], the total reconstructed activity was forced to equal the true total activity.

From several preliminary simulation experiments, it was found that for this joint image reconstruction problem, a simple post-smoothing of the images is not sufficient to suppress

variance differences caused by unmatched convergence of different reconstructions. When the activity image is estimated with known attenuation using MLEM or a similar reconstruction algorithm, it is known that convergence is fast for low spatial frequencies, but takes increasingly longer for higher frequencies. As a result, when two reconstructed images with unmatched convergence are compared, the convergence differences will affect the higher frequencies only. Consequently, these convergence differences can be eliminated by smoothing both images with a low pass filter that suppresses all high frequencies that may be affected by differences in convergence. After such a post-smoothing, the images have a matched spatial resolution and comparison of their variances is meaningful.

For this joint reconstruction problem, smoothing independently the activity and attenuation images is not effective for erasing convergence differences. The reason is probably that there are also noise correlations between the two images, and these correlations are different at different levels of convergence. To suppress those differences, some form of smoothing between the attenuation and activity image would be needed, but it is not clear how this should be done.

Consequently, an attempt was done to obtain approximately matched convergence in both the activity and the attenuation image, by tuning the total number of iterations and the number of attenuation updates per iteration. To estimate convergence, three noise-free sinograms are simulated for a 2D PET system, using an image of 100 $\times$ 100 pixels of 2.5 mm $\times$ 2.5 mm, 100 detectors of 2.5 mm, and 100 angles over 180°, imaging a uniform cylinder with diameter of 20 cm. In the first simulation, the cylinder is perfectly uniform. In the second, a small spot (2x2 pixels) with increased activity is placed in the center. In the third simulation, there is a small spot with increased attenuation in the center. The activity and attenuation images are reconstructed from these sinograms with MLAA. Subtraction of the reconstruction from the first sinogram from the other two produces an image of the small spot, affected by the reconstruction point spread function (PSF) of the activity and attenuation image. From these spot images, we determine the FWHM of the Gaussian post-smoothing kernel that is required to impose a final PSF of 3 pixels FWHM. This is done by adjusting the width of the post-smoothing Gaussian until the post-smoothed spot image reaches the least squares difference from the ground truth spot image, smoothed with a Gaussian of 3 pixels FWHM.

In the experiment, MLAA reconstructions were made for TOF-PET systems with Gaussian TOF-kernel, with a FWHM ranging from 50 to 600 ps FWHM. In addition, also a non-Gaussian TOF-kernel was considered, obtained by summing two Gaussians with 70 and 400 ps FWHM, respectively. Both contributing Gaussians had the same weight (both had an integral equal to 0.5, such that the TOF-kernel integrated to unity). The theory predicts that this non-Gaussian kernel is equivalent to a Gaussian TOF-kernel of 168 ps FWHM, because the integral of the square of these kernels is identical (this is explained in more detail in the Discussion section below). An optimization script was run to determine the number of MLAA iterations and the total number of attenuation updates, which ensured that a Gaussian post-smoothing with a FWHM of (approximately) 2.95 pixels was required to produce a final PSF with 3 pixels FWHM, in the reconstructed activity and attenuation images. The total number of attenuation updates was achieved by applying an almost[2] constant number of MLTR iterations per MLAA iteration. Table 1 shows the results of this experiment.

For each TOF-kernel, 100 Poisson noise realizations of the TOF-PET sinogram were created and reconstructed with MLAA using the iteration scheme of table 1. For all sinograms, the (expectation of) the total number of events was $5.1 \cdot 10^6$. We used the noise-free reconstructions as our estimate of the mean. For each noisy reconstruction, an image of the squared

[2]The number of MLAA iterations may not be a divider of the total number of attenuation updates.

difference with the noise-free reconstruction was computed. The pixel variance was estimated for each noise realisation using all pixels in a central region with 3 cm radius. From the 100 noise realizations, the final variance estimate and its uncertainty (standard deviation) were computed, and converted to relative variances using equations (46) and (47).

The observed variances of the activity and attenuation images were compared for varying TOF resolutions to the model predictions

$$\text{prediction\_}V_\lambda = \frac{\alpha}{\text{SNR}^2_{\text{joint}}} = \frac{\alpha}{\text{SNR}^2_{\lambda,\text{TOF}} - \text{SNR}^2_{\lambda,\text{nonTOF}}} \tag{57}$$

$$\text{prediction\_}V_\mu = \frac{\text{SNR}^2_{\lambda,\text{TOF}}}{\text{SNR}^2_{\lambda,\text{nonTOF}}} \text{prediction\_}V_\lambda \tag{58}$$

where α was a scale factor used to fit both predictions simultaneously to both observed variance curves, by minimizing the weighted squared difference between the variances and their predictions.

4 Results

Table 1 shows the obtained iteration schemes and the required post-smoothing for the eight Gaussian and the non-Gaussian TOF kernels.

Figure 1 shows the relative variances obtained from the noisy reconstructions (solid curves with error bars). The dashed lines show the two curves predicted by (57) and (58). The solid gray curve shows the prediction of the variance in the center of an MLEM reconstruction with known attenuation, which was obtained by deleting the second term of the denominator in (57).

The predicted and observed variances are in good agreement, although the ratio between the observed variances is slightly larger than that between their predictions.

Table 1: *MLAA convergence of the activity and attenuation images for different TOF kernels, expressed as the required post-smoothing FWHM (in pixels) for imposing a final PSF of 3 pixels. Also the number of MLAA iterations and the total number of updates of the attenuation image are listed (columns 2 and 3). The sum-of-Gaussians TOF kernel is indicated with the FWHM of its two Gaussians.*

TOF-kernel (ps)	iterations MLAA	total nr updates of attenuation img	FWHM activity	FWHM attenuation
600	428	1926	2.950	2.948
500	271	1490	2.949	2.950
400	169	1104	2.949	2.950
300	99	863	2.950	2.950
200	52	684	2.951	2.949
168	40	639	2.950	2.950
70 & 400	40	624	2.951	2.949
100	20	547	2.951	2.950
50	8	489	2.949	2.949

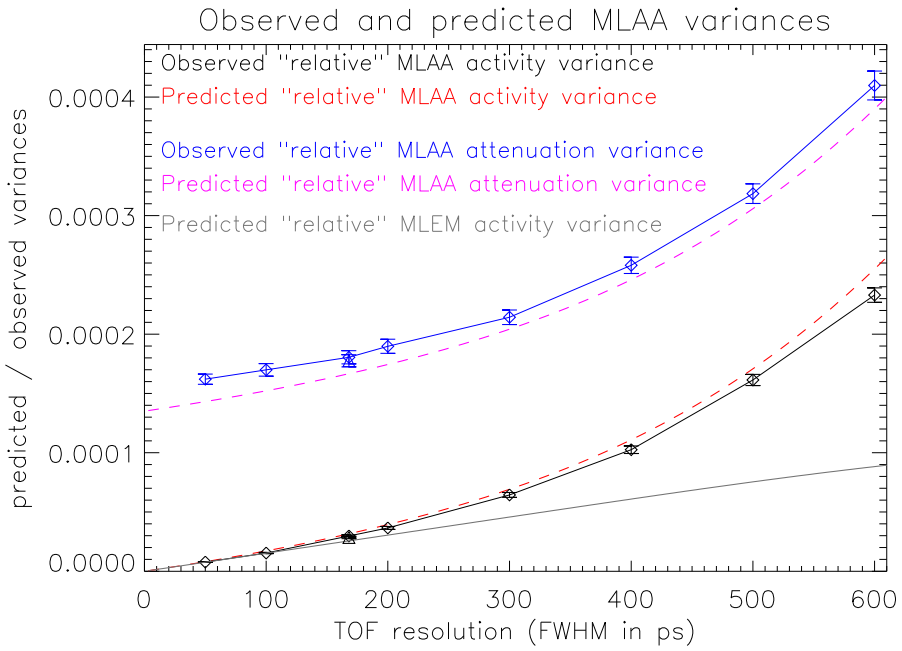

Figure 1: *Plot of the observed and predicted relative variances. A single scale factor was computed to scale the two predicted relative variance curves. Also the predicted variance of the conventional MLEM with known attenuation is shown. The error bars correspond to ± two standard deviations. The triangular points are for the non-Gaussian TOF kernel (combination of 70 ps and 400 ps), they are plotted at the equivalent TOF-resolution of 168 ps (and overlap with the points of the Gaussian TOF-kernel of 168 ps FWHM).*

5 Discussion

It is well known that time-of-flight improves the effective sensitivity of the PET system. However, as stated in [39], "the advantages of TOF are more than a simple increase in effective sensitivity": TOF also leads to a faster and more uniform convergence. In addition, TOF enables the joint reconstruction of attenuation and activity, and here we have shown that improving the TOF resolution also improves the effective sensitivity of the PET system for this joint reconstruction.

We first considered the detection of a weak signal consisting of a known small change of both the activity and the attenuation, using TOF-PET data with an arbitrary TOF-kernel. Our analytical computations showed that the detection SNR (equation (15)) for this detection task is minimized when the signal consisted of a well-matched change to the activity and the attenuation images, given by equation (9). For this particular task, the signal becomes undetectable for non-TOF PET, because the change to the attenuation compensates exactly the change to the activity. This corresponds to the well-known cross-talk problem that hinders joint estimation for non-TOF PET [21, 30, 31]. That same task (9) also minimizes the performance of the detection for TOF-PET, but the minimum SNR, given by (17), is non-zero and improves as the TOF resolution improves and the adverse effects of the cross-talk problem decrease. This agrees with the observation that in early iterations of joint reconstruction from TOF-PET data, the activity and attenuation images suffer from cross-talk, which gradually decreases at higher iterations [40]. Similarly, residual data inconsistencies due to errors in timing calibration, normalization, scatter correction etc. are also seen to produce cross-talk

[30, 40–42].

Tomitani computed the variance in the center of the image of a uniform cylinder, reconstructed from a TOF-PET sinogram, for a PET system with a Gaussian TOF-kernel [15]. This analysis was extended and validated for TOF-PET systems having a distribution of possibly non-Gaussian TOF-kernels in [16]. As a result, for a PET system with multiple TOF-kernels of arbitrary shape, one can compute an equivalent Gaussian TOF-resolution: a conventional TOF-PET system with this equivalent resolution will produce the same variance for the same spatial resolution (in the center of the image) and for the same number of coincident photon pairs.

Here, we have further extended the method to compute the variance in the center of the activity and the attenuation images that are jointly reconstructed from a TOF-PET sinogram. The derivations have been verified with a 2D simulation experiment, comparing the analytical predictions to the observed variances in the reconstructed activity and attenuation images. The agreement is excellent, but not perfect. The discrepancies may be due to the approximate nature of the derivations and/or the incomplete convergence (or convergence match) of the iterative reconstructions.

The experiment included eight Gaussian TOF-kernels and one non-Gaussian kernel. The result confirms that the predictions are valid for TOF-kernels of different shapes. It also confirms that the non-Gaussian TOF-kernel is equivalent to a Gaussian TOF-kernel with a FWHM of 168 ps, as predicted by the theory. MLAA has a very similar convergence for both TOF-kernels, they needed a virtually identical iteration scheme to produce matched convergence (see table 1). And with that iteration scheme, both TOF-PET systems had a virtually identical variance in the reconstructed images (see figure 1).

The analytical result shows that the variances in the activity and attenuation images both depend on the TOF kernel only via the factor $\int k^2(x)dx$, see equations (44) and (45). This implies that if two TOF-PET systems, which differ only by their TOF-kernels, are equivalent for image reconstruction with known attenuation, then they are also equivalent for joint reconstruction of the attenuation and the activity images. And similarly, if a TOF-PET system performs better for reconstruction of the activity with known attenuation, it will also perform better for joint reconstruction of attenuation and activity.

However, the gain achieved by TOF-resolution improvement is different for activity reconstruction and for joint reconstruction. For activity reconstruction with known attenuation, the performance is given by $\mathrm{SNR}^2_{\lambda,\mathrm{TOF}}$, equation (1). When reducing the TOF-kernel width by a factor G, this SNR^2 improves by the same factor G. For joint reconstruction, the variance for the activity image, equation (44), will improve with a factor even higher than G. This is because improving the TOF-resolution not only increases the effective sensitivity, it also decreases the influence of possible cross-talk. On the other hand, the variance for the attenuation image, equation (45), will improve with a factor smaller than G. The reason is that when the TOF-resolution becomes relatively high (compared to the size of the object), the variance in the attenuation image is no longer dominated by the cross-talk from the activity image, but only by the Poisson noise on the acquired PET-data, as is the case in conventional transmission tomography. This slower improvement of the attenuation image is also clear from equation (48), which shows that the ratio between the activity and attenuation variances in joint reconstruction decreases by a factor G when making the TOF-kernel width a factor G smaller.

This is illustrated in figure 2 for four hypothetical PET systems:

1. a system with Gaussian TOF-kernel of 70 ps FWHM,
2. a system with Gaussian TOF-kernel of 400 ps FWHM,

3. a system for which 50% of the events have a TOF-resolution of 70 ps and the other 50% a TOF-resolution of 400 ps, and the TOF-resolution of each event is known,

4. the same system as above, except that it does not identify the TOF-resolution for each event. This system has the non-Gaussian TOF-kernel that was used in the simulation experiment.

Figure 2 shows the TOF-kernels for each system in the first row, and their equivalent Gaussian TOF-kernel in the second. Combining (5), (6) and (55), the FWHM of the equivalent Gaussian TOF kernel was computed as

$$W_3 = \frac{0.644}{\sum_{i=1}^{2} p_i \int_{-\infty}^{\infty} k_i^2(x)dx} \qquad \text{and} \qquad W_4 = \frac{0.664}{\int_{-\infty}^{\infty} (\sum_{i=1}^{2} p_i k_i(x))^2 dx} \tag{59}$$

for the PET systems where the event type could and could not be identified, respectively (see also [16]). Inserting Gaussian TOF-kernels with FWHM $W_1 = 70$ ps and $W_2 = 400$ ps, setting $p_1 = p_2 = 0.5$ and using (46) of [16], one obtains

$$W_3 = \frac{1}{\frac{p_1}{W_1} + \frac{p_2}{W_2}} = 119 \text{ ps} \qquad \text{or} \qquad W_4 = \frac{1}{\frac{p_1^2}{W_1} + \frac{p_2^2}{W_2} + 2\sqrt{2}\frac{p_1 p_2}{\sqrt{W_1^2+W_2^2}}} = 168 \text{ ps}. \tag{60}$$

The figure also reports the relative variances, normalized to the variance for activity reconstruction of the 70 ps TOF-PET system.

The figure shows that for a 70 ps TOF-PET system, the variance in the activity image only increases with 10% if one jointly reconstructs the attenuation image too. For 400 ps, this increase is 75%. Figure 1 shows that as the TOF-resolution approaches perfection, the variance increase caused by jointly estimating the attenuation vanishes. Figure 2 also shows that if the mixed 70 and 400 ps events can be labeled with their individual TOF-resolution, the equivalent Gaussian TOF-resolution improves from 168 ps to 119 ps. The variance in the activity image improves with the same factor for conventional reconstruction, and with a higher factor for joint reconstruction. The variance in the jointly reconstructed attenuation image improves with a much smaller factor. The same pattern, but with larger factors, is seen when going from 70 to 400 ps (equivalent) TOF-resolution. Note that, if the TOF-kernel is small compared to the object, the improvement for activity reconstruction only depends on the TOF-kernel, whereas the improvement for joint reconstruction also depends on the diameter of the uniform cylinder. This is because $\text{SNR}^2_{\text{joint}} = \text{SNR}^2_{\lambda,\text{TOF}} - \text{SNR}^2_{\lambda,\text{nonTOF}}$, and the ratio of the TOF and non-TOF SNRs depends on the object size.

The system comparison presented here focuses on the TOF-kernel(s), we assume that all other system features are identical. In real PET systems, systems with different TOF-resolution are likely to differ also in other respects, such as solid angle, stopping power, spatial resolution and energy resolution. All these other features must of course be taken into account too when comparing real PET systems for particular imaging tasks.

6 Conclusion

The proposed analysis shows that if two TOF-PET systems, which differ only by their TOF-kernels, are equivalent for image reconstruction with known attenuation, then they are also equivalent for joint reconstruction of the activity and the attenuation images. And similarly, if a TOF-PET system performs better for reconstruction of the activity image with known attenuation, it will also perform better for joint reconstruction of activity and attenuation.

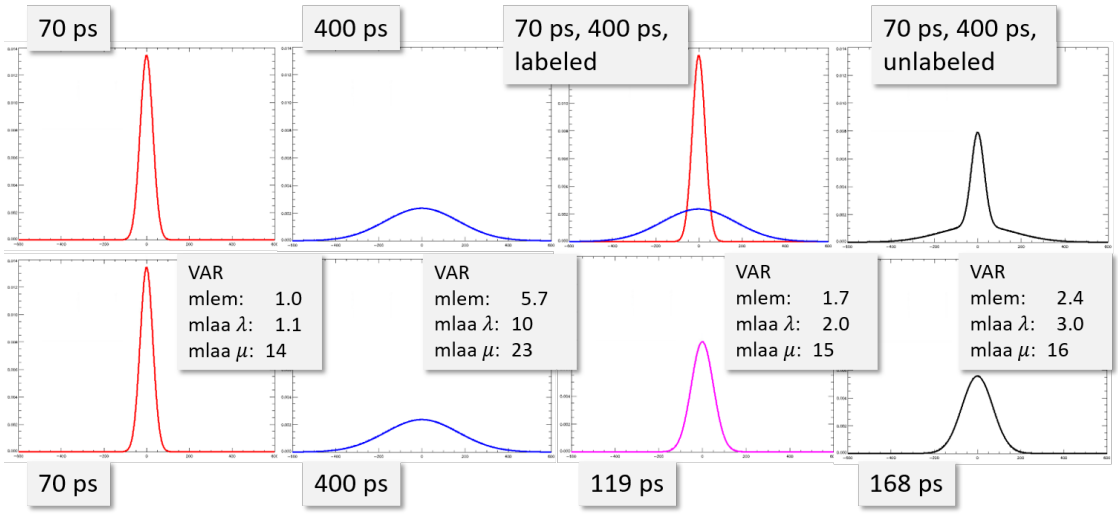

Figure 2: *First row shows four TOF-PET systems having a different combination of Gaussian TOF-kernels: always 70 ps, always 400 ps, 50% 70 ps and 50% 400 ps with identified TOF-kernel for each event, 50% 70 ps and 50% 400 ps and TOF-kernel not identified per event. Second row shows the corresponding equivalent Gaussian TOF-kernel, and the variance in the images obtained with conventional MLEM (with known attenuation) or with joint reconstruction of the activity and attenuation images. These variances are normalized to the variance obtained with conventional MLEM for a Gaussian TOF-kernel with 70 ps FWHM. This was done for a cylinder of 20 cm diameter.*

However, the gain achieved by TOF-resolution improvements is different for activity reconstruction and for joint reconstruction.

As already reported in our previous paper [16], we find that the integral of the square of the TOF-kernel is an appropriate metric of the time-of-flight resolution, because in contrast to the FWHM or the standard deviation, the integral of the square accounts for the entire shape of the TOF-kernel.

References

[1] J. Van Sluis, J. De Jong, J. Schaar, et al. "Performance characteristics of the digital Biograph Vision PET/CT system". In: *Journal of Nuclear Medicine* 60.7 (2019), pp. 1031–1036.

[2] P. Lecoq, C. Morel, J. O. Prior, et al. "Roadmap toward the 10 ps time-of-flight PET challenge". In: *Physics in Medicine & Biology* 65.21 (2020), 21RM01.

[3] D. R. Schaart. "Physics and technology of time-of-flight PET detectors". In: *Physics in Medicine & Biology* 66.9 (2021), 09TR01.

[4] S. I. Kwon, E. Roncali, A. Gola, et al. "Dual-ended readout of bismuth germanate to improve timing resolution in time-of-flight PET". In: *Phys Med Biol* 64.10 (2019), p. 105007.

[5] E. Roncali, S. I. Kwon, S. Jan, et al. "Cerenkov light transport in scintillation crystals explained: realistic simulation with GATE". In: *Biomed Phys Eng Express* 5.3 (2019), p. 035033.

[6] G. Ariño-Estrada, E. Roncali, A. R. Selfridge, et al. "Study of Čerenkov Light Emission in the Semiconductors TlBr and TlCl for TOF-PET". In: *IEEE Trans Radiat Plasma Med Sci* 5.5 (2020), pp. 630–637.

[7] N. Kratochwil, S. Gundacker, P. Lecoq, et al. "Pushing Cherenkov PET with BGO via coincidence time resolution classification and correction". In: *Phys Med Biol* 65.11 (2020), p. 115004.

[8] N. Efthimiou, N. Kratochwil, S. Gundacker, et al. "TOF-PET image reconstruction with multiple timing kernels applied on Cherenkov radiation in BGO". In: *IEEE transactions on radiation and plasma medical sciences* 5.5 (2020), pp. 703–711.

[9] S. Gundacker, R. M. Turtos, N. Kratochwil, et al. "Experimental time resolution limits of modern SiPMs and TOF-PET detectors exploring different scintillators and Cherenkov emission". In: *Physics in Medicine & Biology* 65.2 (2020), p. 025001.

[10] D Yvon, V Sharyy, M Follin, et al. "Design study of a "scintronic" crystal targeting tens of picoseconds time resolution for gamma ray imaging: the ClearMind detector". In: *Journal of Instrumentation* 15.07 (2020), P07029.

[11] R Ota, K Nakajima, I Ogawa, et al. "Coincidence time resolution of 30 ps FWHM using a pair of Cherenkov-radiator-integrated MCP-PMTs". In: *Physics in Medicine & Biology* 64.7 (2019), 07LT01.

[12] G Razdevšek, R Pestotnik, P Križan, et al. "Exploring the Potential of a Cherenkov TOF PET Scanner: A Simulation Study". In: *IEEE Transactions on Radiation and Plasma Medical Sciences* 7.1 (2022), pp. 52–61.

[13] R. M. Turtos, S Gundacker, E Auffray, et al. "Towards a metamaterial approach for fast timing in PET: experimental proof-of-concept". In: *Phys Med Biol* 64.18 (2019), p. 185018.

[14] G Konstantinou, P Lecoq, J. Benlloch, et al. "Metascintillators for ultra-fast gamma detectors: a review of current state and future perspectives". In: *IEEE Trans Radiat Plasma Med Sci* 6.1 (2021), pp. 5–15.

[15] T. Tomitani. "Image reconstruction and noise evaluation in photon time-of-flight assisted positron emission tomography". In: *IEEE Trans Nucl Science* NS-28.6 (1981), pp. 4582–4589.

[16] J. Nuyts, M. Defrise, S. Gundacker, et al. "The SNR of positron emission data with Gaussian and non-Gaussian time-of-flight kernels, with application to prompt photon coincidence". In: *IEEE Transactions on Medical Imaging* (2022).

[17] N. Cao, R. H. Huesman, W. W. Moses, et al. "Detection performance analysis for time-of-flight PET". In: *Physics in Medicine & Biology* 55.22 (2010), p. 6931.

[18] L. Eriksson and M. Conti. "Randoms and TOF gain revisited". In: *Physics in Medicine & Biology* 60.4 (2015), p. 1613.

[19] X. Zhang, R. D. Badawi, S. R. Cherry, et al. "Theoretical study of the benefit of long axial field-of-view PET on region of interest quantification". In: *Physics in Medicine & Biology* 63.13 (2018), p. 135010.

[20] X. Zhang, Q. Peng, J. Zhou, et al. "Lesion detection and quantification performance of the Tachyon-I time-of-flight PET scanner: phantom and human studies". In: *Physics in Medicine & Biology* 63.6 (2018), p. 065010.

[21] J. Nuyts, P. Dupont, S. Stroobants, et al. "Simultaneous maximum a posteriori reconstruction of attenuation and activity distributions from emission sinograms". In: *IEEE transactions on medical imaging* 18.5 (1999), pp. 393–403.

[22] M Landmann, S. Reske, and G Glatting. "Simultaneous iterative reconstruction of emission and attenuation images in positron emission tomography from emission data only". In: *Medical Physics* 29.9 (2002), pp. 1962–1967.

[23] F. Natterer and H. Herzog. "Attenuation correction in positron emission tomography". In: *Mathematical Methods in the Applied Sciences* 15 (1992), pp. 321–330.

[24] S. H. Manglos and T. M. Young. "Constrained IntraSPECT reconstruction from SPECT projections". In: *1993 IEEE Conference Record Nuclear Science Symposium and Medical Imaging Conference*. IEEE. 1993, pp. 1605–1609.

[25] A. Krol, J. E. Bowsher, S. H. Manglos, et al. "An EM algorithm for estimating SPECT emission and transmission parameters from emission data only". In: *IEEE transactions on medical imaging* 20.3 (2001), pp. 218–232.

[26] A. R. De Pierro and F. Crepaldi. "Activity and attenuation recovery from activity data only in emission computed tomography". In: *Computational & Applied Mathematics* 25.2-3 (2006), pp. 205–227.

[27] M. Defrise. "Simultaneous estimation of activity and attenuation in classical PET: Uniqueness issues". In: *2016 IEEE Nuclear Science Symposium, Medical Imaging Conference and Room-Temperature Semiconductor Detector Workshop (NSS/MIC/RTSD)*. IEEE. 2016, pp. 1–3.

[28] F. Crepaldi and A. R. De Pierro. "Activity and attenuation reconstruction for positron emission tomography using emission data only via maximum likelihood and iterative data refinement". In: *IEEE Transactions on Nuclear Science* 54.1 (2007), pp. 100–106.

[29] A. Mihlin and C. S. Levin. "An expectation maximization method for joint estimation of emission activity distribution and photon attenuation map in PET". In: *IEEE transactions on medical imaging* 36.1 (2016), pp. 214–224.

[30] A. Salomon, A. Goedicke, B. Schweizer, et al. "Simultaneous reconstruction of activity and attenuation for PET/MR". In: *IEEE transactions on medical imaging* 30.3 (2011), pp. 804–813.

[31] M. Defrise, A. Rezaei, and J. Nuyts. "Time-of-flight PET data determine the attenuation sinogram up to a constant". In: *Phys Med Biol* 57.4 (2012), p. 885.

[32] A. Rezaei, M. Defrise, G. Bal, et al. "Simultaneous reconstruction of activity and attenuation in time-of-flight PET". In: *IEEE transactions on medical imaging* 31.12 (2012), pp. 2224–2233.

[33] Y. Berker and Y. Li. "Attenuation correction in emission tomography using the emission data - a review". In: *Medical physics* 43.2 (2016), pp. 807–832.

[34] H. H. Barrett, J. Yao, J. P. Rolland, et al. "Model observers for assessment of image quality". In: *Proc Natl Acad Sci USA* 90.21 (1993), pp. 9758–9765.

[35] J. A. Fessler and W. L. Rogers. "Spatial resolution properties of penalized-likelihood image reconstruction: space-invariant tomographs". In: *IEEE Transactions on Image processing* 5.9 (1996), pp. 1346–1358.

[36] J. A. Fessler and S. D. Booth. "Conjugate-gradient preconditioning methods for shift-variant PET image reconstruction". In: *IEEE transactions on image processing* 8.5 (1999), pp. 688–699.

[37] H. Shi and J. A. Fessler. "Quadratic regularization design for fan beam transmission tomography". In: *Medical Imaging 2005: Image Processing*. Vol. 5747. SPIE. 2005, pp. 2023–2033.

[38] J. Qi and R. M. Leahy. "Resolution and noise properties of MAP reconstruction for fully 3-D PET". In: *IEEE transactions on medical imaging* 19.5 (2000), pp. 493–506.

[39] J. S. Karp, S. Surti, M. E. Daube-Witherspoon, et al. "Benefit of time-of-flight in PET: experimental and clinical results". In: *Journal of Nuclear Medicine* 49.3 (2008), pp. 462–470.

[40] Y. Li, S. Matej, and J. S. Karp. "Practical joint reconstruction of activity and attenuation with autonomous scaling for time-of-flight PET". In: *Physics in Medicine & Biology* 65.23 (2020), p. 235037.

[41] J. Nuyts, A. Rezaei, and M. Defrise. "The validation problem of joint emission/transmission reconstruction from TOF-PET projections". In: *IEEE Transactions on Radiation and Plasma Medical Sciences* 2.4 (2018), pp. 273–278.

[42] A. Rezaei, G. Schramm, K. Van Laere, et al. "Estimation of crystal timing properties and efficiencies for the improvement of (joint) maximum-likelihood reconstructions in TOF-PET". In: *IEEE transactions on medical imaging* 39.4 (2019), pp. 952–963.